

Realization of Landau-Zener Rabi Oscillations on optical lattice clock

Wei Tan,^{1,2} Wei-Xin Liu,³ Ying-Xin Chen,^{1,2,4} Chi-Hua Zhou,¹
Guo-Dong Zhao,^{1,2,4} Hong Chang,^{1,2,4,*} and Tao Wang^{5,6,†}

¹*Key Laboratory of Time and Frequency Primary Standards,
National Time Service Center, Chinese Academy of Sciences, Xi'an 710600, China*

²*Hefei National Laboratory, Hefei 230088, China*

³*Department of Physics, Xinzhou Normal University, Xinzhou 034000, China*

⁴*School of Astronomy and Space Science, University of Chinese Academy of Sciences, Beijing 100049, China*

⁵*Department of Physics, and Chongqing Key Laboratory for Strongly Coupled Physics,
Chongqing University, Chongqing, 401331, China*

⁶*Center of Modern Physics, Institute for Smart City of Chongqing University in Liyang, Liyang, 213300, China*

Manipulating quantum states is at the heart of quantum information processing and quantum metrology. Landau-Zener Rabi oscillation (LZRO), which arises from a quantum two-level system swept repeatedly across the avoided crossing point in the time domain, has been suggested for widespread use in manipulating quantum states. Cold atom is one of the most prominent platforms for quantum computing and precision measurement. However, LZRO has never been observed in cold atoms due to its stringent requirements. By compensating for the linear drift of the clock laser and optimizing experimental parameters, we successfully measured LZRO on the strontium atomic optical clock platform under both fast and slow passage limits within 4 to 6 driving periods. Compared to previous results on other platforms, the duration of the plateau is 10^4 times longer in the optical lattice clock. The experimental data also suggest that destructive Landau-Zener interference can effectively suppress dephasing effects in the optical lattice clock, paving the way for manipulating quantum states against various environmental effects in cold atomic systems.

Keywords: optical lattice clock, Landau-Zener-Stückelberg-Majorana interference, Rabi oscillation

I. INTRODUCTION

Cold atom is among the most promising candidates for quantum computing and plays important roles in the precise measurement of acceleration, electric and magnetic fields, time, frequency, and more [1–5]. Manipulating the quantum states of atoms, typically using Rabi oscillation excited by external laser or microwave fields, is a key step in all these applications. However, due to various dephasing effects, it is challenging to control the state universally in an atomic ensemble. For example, in atoms trapped in a harmonic trap at finite temperatures, the atom-laser coupling strength varies with the motional state quantum number due to coupling with phonons. This variation makes it difficult to apply a perfect $\pi/2$ pulse to all the atoms, thereby degrading the precision of Ramsey-type interferometers.

Landau-Zener-Stückelberg interference appears when modulating two energy states to traverse the avoided level crossing points periodically [6–24]. If the interference is allowed to occur at multiple consecutive Landau-Zener (LZ) transitions, periodic oscillations of the population in different energy levels will occur, which is similar to the Rabi oscillation [25–27]. This kind of time-domain oscillation is usually named Landau-Zener-Rabi oscillation (LZRO). LZROs have been proven to be against various dephasing effects and have been widely used in

manipulating quantum states globally for electric spin, quantum dot and NV center [2, 3, 28, 29]. Thus, it is natural to generate this method for cold atom systems. However, the realization of LZROs requires strict experimental conditions that the physical system needs a long coherence time for the long sequence of Landau Zener process. At present, it has never been obtained in the cold atomic system.

On the optical clock platform, the transition between the two clock states $|0\rangle$ and $|1\rangle$ belongs to the dipole forbidden transition, and the clock laser used for detection also has a long enough coherent time [30, 31], which provides a good opportunity for the detection of LZRO. Another point of benefit is that the atoms are in a light trap of magic wavelengths, thus the construction of the Hamiltonian quantity can be very precise [32]. The LZ Hamiltonian can be realized on optical clock platform by periodic modulating transition frequency [33–35].

However, the drift of the clock laser could still be a challenge for detecting LZRO, which requires the fixed detuning. In this paper, we compensated the linear drift of the clock laser and chose the system parameter to minimize the effect on LZRO for non-linear drift. An external frequency modulation of time synchronization is added to the frequency of clock laser by an acousto-optic modulator (AOM), which can achieve accurate modulation frequency, amplitude, and phase. Within the above operation, the LZRO is detected on the strontium atomic optical clock platform under the fast and slow passage limit.

Our paper is organized as follows. In Section II, we described the experimental setup and theoretical princi-

* corresponding author: changhong@ntsc.ac.cn

† corresponding author: tauwaang@cqu.edu.cn

ple for LZRO. In Section III, we discuss the experimental results. In Section IV, we present our main conclusions.

II. EXPERIMENTAL SETUP AND PRINCIPLE

Optical lattice clock system could be described as an ensemble of two level atoms trapped in identical harmonic traps formed by 'magical wavelength' lattice laser, and an ultra-narrow clock laser excited the atoms from ground state (1S_0) to the long lived state (3P_0) [30, 31]. In our experiments, Approximately 10^4 ^{87}Sr atoms were trapped in an optical lattice with a trap depth of 90 Er , in which Er means recoil energy. The axial and radial temperature of the cold atoms were 4.7 μK and 6.3 μK , respectively. The longitude modulation of Landau-Zener Hamiltonian was obtained by periodically driving the clock laser frequency. To stabilize the driving phase of 698 nm clock laser, an important factor for the experiments, we implemented the driving by using a burst-mode sinusoidal low-frequency signal delivered to the laser frequency via an AOM. The burst pulse was triggered by the clock sequence. This setup allows convenient and accurate adjustment of parameters such as frequency, amplitude, and initial phase of the modulation waveform. The device schematic diagram is shown in Fig. 1(a).

Under the modulation, the form of the clock laser becomes $\cos [f(\omega_p - A\omega_s \cos \omega_s t) dt]$, where the A and ω_s are respectively the amplitude and the frequency of the modulation signal, ω_p is the average clock laser frequency. After transforming to a proper rotating frame and applying the rotating-wave approximation, the Hamiltonian for the dynamics of clock states becomes

$$\hat{H}_{\vec{n}}(t) = \frac{\hbar}{2} [\delta + A\omega_s \cos(\omega_s t)] \hat{\sigma}_z + \frac{\hbar g_{\vec{n}}}{2} \hat{\sigma}_x, \quad (1)$$

where \hbar is the Planck constant, $\delta = \omega_0 - \omega_p$ is the clock laser detuning. $\hat{\sigma}_{z(x)}$ is the Pauli matrix, and

$$g_{\vec{n}} = g L_{n_z}(\eta_z^2) L_{n_x}(\eta_x^2) e^{-\eta_z^2/2} e^{-\eta_x^2/2} \quad (2)$$

is the modified coupling strength of clock laser to clock transition at external eigenstates $\vec{n} = (n_z, n_x)$. $\eta_z = 0.25$ and $\eta_x = 0.022$ are the longitudinal and transverse Lamb-Dicke parameters, respectively. $L_n(\cdot)$ is the n th order Laguerre polynomial.

When the longitudinal term of Hamiltonian Eq. (1) approaches zero, the energy spectrum experience an avoided crossing point, thus the LZ transition occurs, as shown in Fig. 1(b). Assuming the system is initialized in the ground state, the probability of the system still in the ground state after avoided crossing point is given by the so-called LZ formula

$$P_{LZ} = \exp\left(-\frac{\pi g_{\vec{n}}^2}{2v}\right) \quad (3)$$

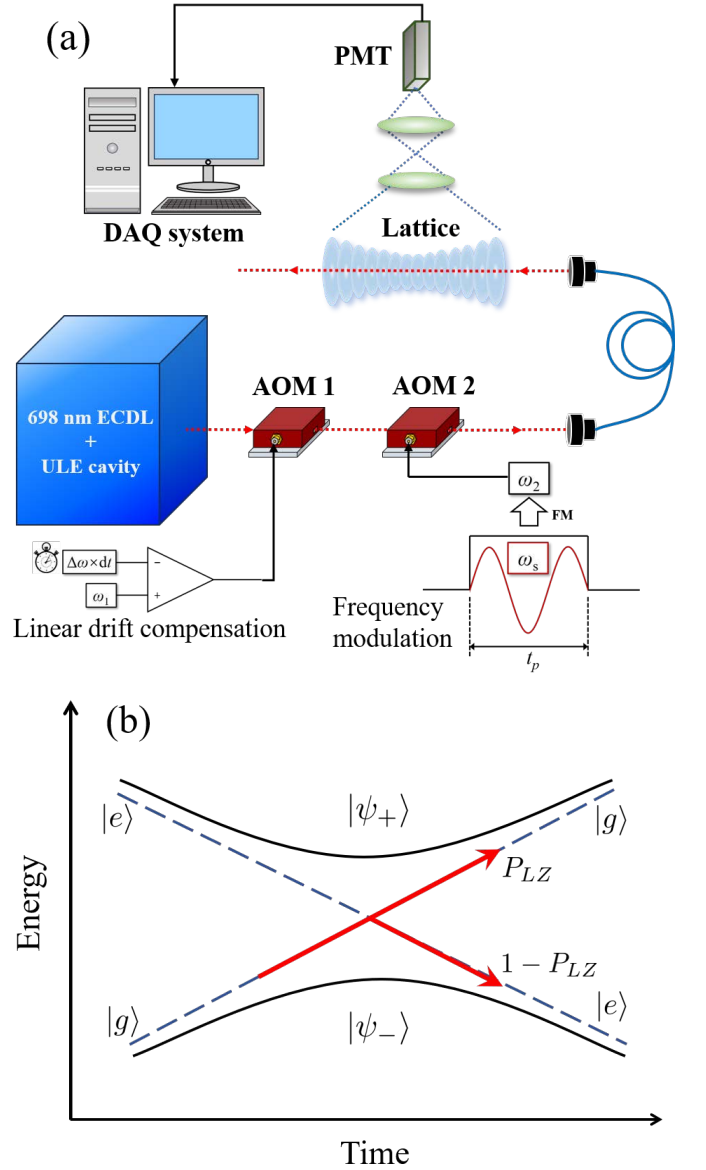


FIG. 1. (a) Experimental scheme. The polarization directions of the 813.43 nm magic wavelength lattice light and the clock laser are perpendicular to the ground and coincide. The diameter of the 698.45 nm clock laser beam is around 800 μm , which is much larger than the lattice beam waist diameter. The 698 nm external cavity diode laser (ECDL) is locked onto a 10 cm ULE glass cavity using Pound-Drever-Hall (PDH) methods. The gate modulation is triggered by the data acquisition (DAQ) system, and its width can be set manually. The lattice imaging lens, composed of two lenses, converges weak lattice signals onto the photomultiplier tube (PMT), and the detected signals are recorded by the data acquisition and processing system. (b) Schematic diagram of LZ transition. The dashed lines represent the diabatic energy levels, while the solid lines represent the adiabatic energy levels. When the system's energy levels undergo an avoided crossing, a non-adiabatic transition occurs between the adiabatic states, as given by Eq.(3).

with $v = A\omega_s^2$, which is the sweep rate of energy levels at the avoided crossing point for the zero-detuning [32]. Among LZ transitions between two avoided crossing points, the evolution of the system is assumed to adiabatically follow the instantaneous eigenstates of Hamiltonian Eq. (1), thus acquiring different phases for the ground and excited paths. Each LZ transition brings atom waves in the two paths together, leading to interference. Repeatedly sweeping across the avoided crossing point in time zone will induce LZRO between different energy levels. For LZRO, it is convenient to define two bases: the adiabatic basis, which consists of the instantaneous eigenstates and is labeled as $|-\rangle$ and $|+\rangle$; and the diabatic basis, which consists of the ground and excited states of atoms and is labeled as $|g\rangle$ and $|e\rangle$. These two bases can be transformed into each other. In experiments, the atomic population probability in the diabatic basis can be detected. Based on this, the corresponding population probability in the adiabatic basis can be calculated.

Detecting LZRO requires fixed detuning $\delta = 0$, which is challenging for our system due to the uncontrollable drift of the clock laser. For conventional Rabi oscillation, the zero detuning point is determined from the symmetric Rabi spectrum at a fixed probing time. However, this method fails for detecting LZRO, as the Rabi spectrum is no longer symmetric with $\delta = 0$. Therefore, to achieve fast and precise detection of LZRO, it is essential to stabilize the center frequency of the clock laser. Based on our loop-on experiments, we observed a slow variation in the frequency drift rate of the clock laser, ranging from 0.06 to 0.09 Hz/s over one day, see Appendix A for more details. This drift is caused by variations in the eigenfrequency of the ultra-low expansion (ULE) cavity due to factors such as temperature, humidity, and vacuum conditions. Fortunately, the frequency drift over a two-hour period generally follows a linear trend. Short-term frequency fluctuations (with a stability of less than $5.0E-15$ at 1s) mainly arise from vibrations and impose limits on the linewidth of the ULE cavity. By optimizing the Fourier limit of the clock transition line, it is possible to reduce the impact of short-term frequency noise on LZRO. To achieve this, a fixed stepped linear drift compensation is applied to AOM1. This compensation, implemented through a loop-on per-measurement approach, helps maintain a fixed-detuning position for the center frequency of the clock laser throughout the entire duration of the experiment.

III. RESULTS AND DISCUSSIONS

For LZRO, two limiting cases named fast-passage limit ($1 - P_{LZ} \ll 1$) and slow-passage limit ($P_{LZ} \ll 1$) are special examples that exhibit distinct oscillation behavior. Specifically, in the fast-passage limit, the system evolves through the diabatic states $|g\rangle$ and $|e\rangle$, while in the slow-passage limit, the system follow the adiabatic states $|-\rangle$

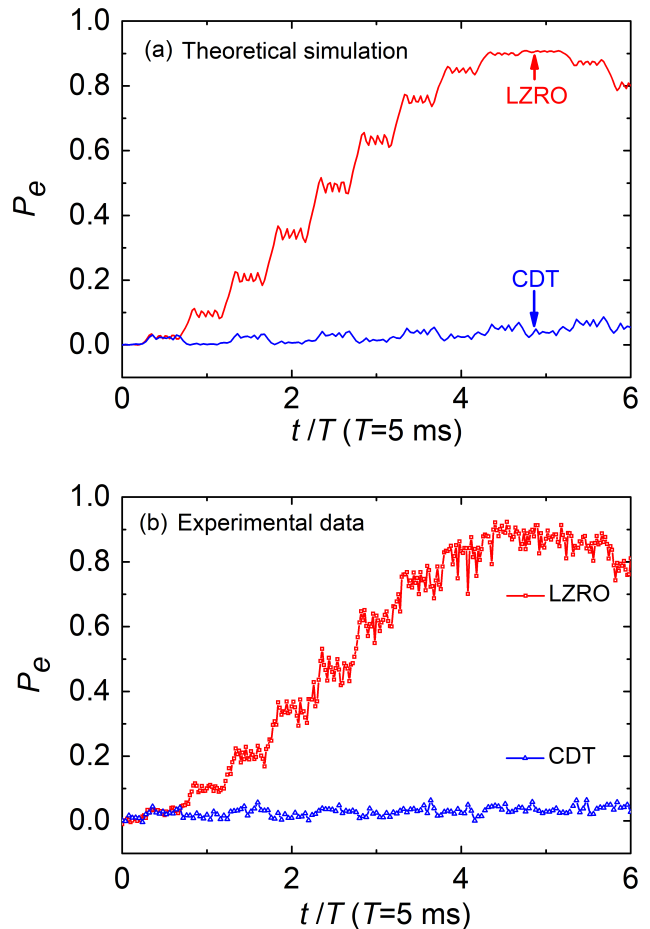


FIG. 2. The dependence of Excitation rate of the clock transition on the detection time t in the fast-passage limit. Six oscillation periods were performed, each with a period of 5 ms. (a) Theoretical numerical simulation results. The LZRO and CDT spectra are plotted (LZRO in red and CDT in blue). (b) Experimental data. The upper red line represents the constructive LZRO spectrum, while the lower blue line represents the destructive spectrum corresponding to CDT.

and $|+\rangle$. When the system sweeps across the avoided crossing points repeatedly, the phase accumulated during the evolution will induce constructive and destructive interference, which is reflected in the oscillation behavior between the two diabatic or adiabatic states [22, 25, 26]. We first measured the constructive and destructive interference induced by a sequence of LZ transitions under fast-passage limit. In this experiment, the parameter g was tuned to near 120 by carefully adjusting the incident 698 nm laser power, and set $2\pi g/\omega_s = 0.6$. When the modulation amplitude A was closing to 13.3 and 11.55, giving $P_{LZ} \approx 0.97$ (fast-passage regime), the LZ interferences satisfied the conditions for constructive and destructive interference, respectively.

We can see from the experimental results shown in Fig. 2(b) that the constructive interference induced LZROs (upper data) with obvious step-like structures, which

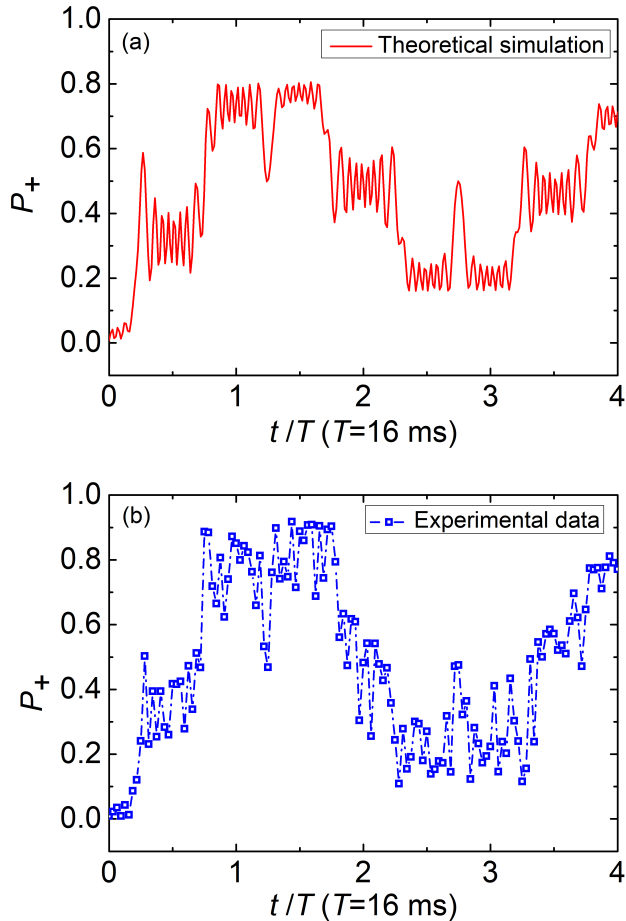


FIG. 3. Constructive interference in the slow-passage limit over 4 driving periods. The dependence of the excitation rate of the clock transition in the adiabatic basis on the driving period t in (a) theoretical simulation and (b) experimental data.

agrees well with the numerical simulation Fig. 2(a)(solid red LZRO line). The step-like structure could be interpreted as following: between two adjacent LZ transitions, atoms adiabatically follow the adiabatic bases, which is very close to the diabatic bases under the experimental parameter. Thus the atom population probability in states $|e\rangle$ is almost constant between two adjacent LZ transitions. The experimental data in Fig. 2 also show that the step structure is very clear within four driving periods but becomes obscure with longer evolution times. The reason for this might be the non-linear drift of the clock laser. Under destructive interference in the fast-passage limit, atoms are frozen in the initial state for each LZ transition, resulting in the coherent destructive tunneling (CDT) phenomenon. This is illustrated in the lower parts of Fig. 2(a) and (b) for the numerical and experimental results, respectively.

Now we turn to the slow-passage limit. In this case, we set g near to 320 and ω_s to $2\pi \times 62.5$ Hz. Then we measured four driving-periods interference spectrum.

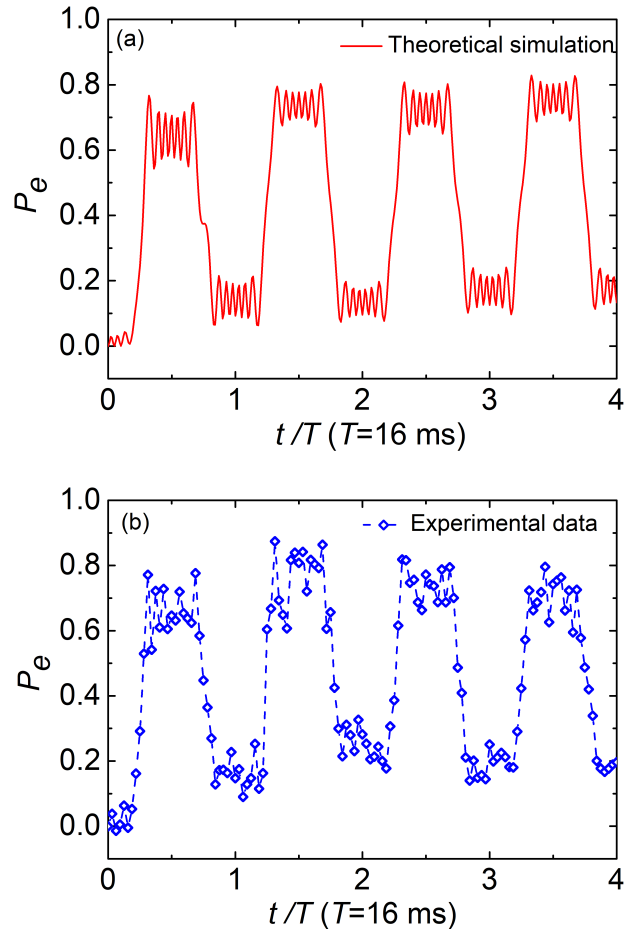


FIG. 4. Destructive interference at the slow-passage limit. The dependence of excitation rate of the clock transition on the driving period t in diabatic basis under $g=320$ Hz, $A=20.6$. (a) The numerical simulation results. (b) The experimental results.

The constructive and destructive LZROs were detected under $A = 22.2$ and 20.6 , respectively, which give $P_{LZ} \approx 0.24$ (slow-passage regime).

For the constructive interference, the oscillation behavior is irregular in the diabatic basis. However, when converting the results to the adiabatic basis, the global interference becomes clearly recognizable. The coarse-grained oscillating behavior in the adiabatic basis shows an explicit LZRO pattern within four driving periods, as shown with in Fig. 3(b), which is consistent with the numerical simulation presented in Fig. 3(a). However, after two periods, the fluctuation of each plateau is much larger than predicted by the theoretical simulation, which might be due to the non-linear drift of the clock laser.

For the destructive interference, because the LZ transition probability is very small, atoms remain in the ground state of the adiabatic basis. When converted to the diabatic basis, the atom population changes dramat-

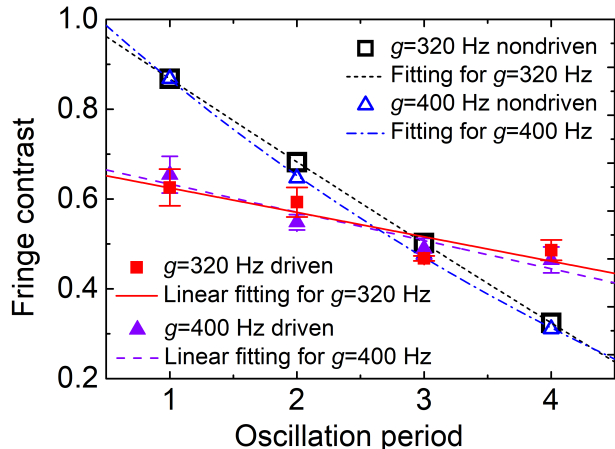


FIG. 5. Comparison of fringe contrast between nondriven Rabi oscillations (black hollow square with $g=320$ Hz and blue hollow triangle with $g=400$ Hz) and LZ destructive interference spectra (red solid square and solid violet triangle) in slow-passage limit under $g=320$ Hz and $A=20.6$, and $g=400$ Hz and $A=21.4$, respectively. The LZ destructive interference spectra exhibit quite slow decay rate with -0.051 and -0.059 at $g=320$ Hz and $g=400$ Hz, respectively. The exponential fitting ($fringecontrast = offset + D \exp(-t/v)$) for the nondriven fringe contrast show decay constants v of 45.77 for $g=320$ Hz and 6.40 for $g=400$ Hz

ically between two plateaus, as shown in Fig. 4(a) and (b). The experimental data agree very well with the numerical simulation within four driving periods, except that the oscillation of each plateau is much larger than theoretically predicted. The drastic oscillation between two plateaus can be interpreted as follows: the adiabatic ground state swaps between the diabatic ground and excited states at each level avoided crossing point.

Moreover, we quantified the dephasing effect under destructive interference conditions within four periods by analyzing the contrast fringe. As shown in Fig. 5, the decay of the contrast fringe for two different Rabi coupling strength cases can both be fitted by a slow slope linear function. To compare this with Rabi oscillation, we also measured the contrast fringe within four driving periods under the same experimental conditions, which indicates a fast exponential decay behavior, as shown in Fig. 5. One can clearly observe a suppression of dephasing by LZRO. Our system can be considered a Landau-Zener interferometer with uncontrollable noise (non-linear drift); thus, we have demonstrated that LZRO can even suppress dephasing without perfect conditions. The comparison between LZRO and Rabi oscillation for the same measurement time can be found in Appendix B, which provides a more direct indication of the slow decay of LZRO and the fast decay of Rabi oscillation.

IV. CONCLUSION AND OUTLOOK

In this paper, we observe the LZRO in a ^{87}Sr optical lattice clock platform using Rabi spectroscopy, by compensating for the linear drift of the clock laser and carefully selecting system parameters. Under fast-passage conditions, the LZRO spectrum for coherent constructive interference manifests as a coarse-grained, step-like oscillation, while coherent destructive interference reveals a CDT effect. In slow-passage conditions, the experimental results for coherent constructive interference also show a coarse-grained, step-like oscillation but are observed in adiabatic rather than diabatic bases. For coherent destructive interference under slow-passage conditions, the atomic population probability oscillates between two widely separated values, each lasting half a period. No decay effect is observed in the spectrum, even with increasing Rabi coupling strength.

Currently, we can only obtain clear LZRO data within 4 driving periods due to the non-linear drift of the clock laser. However, the plateau of the step-like spectrum persists for several milliseconds, which is 10^4 times longer than in previous NV center experiments [29], thanks to the long coherence time of the optical clock platform. This advantage allows for precise atomic state manipulation, enabling atoms with a broad range of Rabi coupling strengths to approach nearly the same quantum state with a single pulse.

Further work is needed to achieve high-precision quantum state control in atomic ensembles, including reducing non-linear drift effects to extend the number of detectable driving periods and minimizing plateau oscillations.

ACKNOWLEDGMENTS

This work was supported by the Strategic Priority Research Program of the Chinese Academy of Sciences (Grant No. XDB35010202) and the National Natural Science Foundation of China under Grant No. 12274045, No. 12274046, No.12347101 and No. 12203057.

Appendix A: Linear drift of clock laser

To enable the rapid detection of LZRO, two AOMs are used in the experiment to achieve line drift compensation and frequency modulation of the clock laser, respectively. The sum of the carrier frequencies of the two AOMs equals the difference between the ULE cavity mode frequency and the clock transition frequency. By feedback control in the optical clock system, the linear drift rate of the clock laser varies slowly between 0.06 and 0.09 Hz/s. In Fig. 6, we show the frequency drift measured near 20 minutes. Due to daily variations in laboratory temperature, humidity, and other environmental

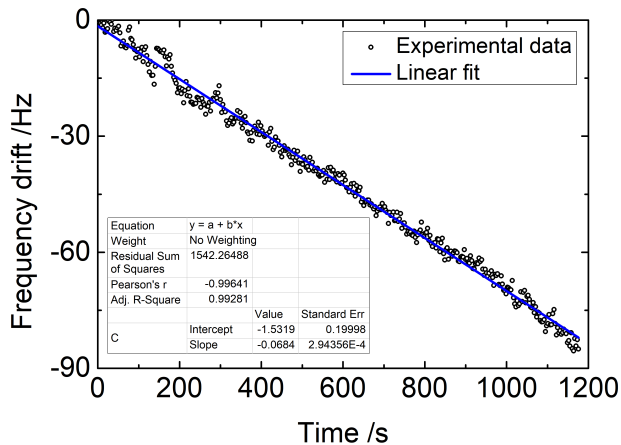


FIG. 6. Frequency drift of clock laser. After the clock laser was locked to the transition line, the output frequency of the feedback AOM was recorded, allowing us to measure the frequency drift of the clock laser. This figure shows the frequency variation over a 20-minute period. According to the linear fit, the drift rate is 0.0684 Hz/s. Due to phase noise and feedback loop system noise, the data exhibits short-term frequency fluctuations of ± 3 Hz.

factors, the drift rate of the ULE cavity is slightly different each day. However, the frequency shift over a two-hour period generally follows a linear trend. Therefore, applying a fixed period of linear drift compensation to AOM1 can maintain the clock laser at a fixed-detuning position relative to the clock transition spectrum during the experimental period. The LZRO spectrum can be quickly obtained by gradually increasing the clock laser detection time sequentially. Additionally, scanning the clock laser frequency can facilitate the detection of LZ interferences.

Appendix B: Comparison between the destructive interference LZRO in slow-passage limit and the Rabi oscillation on nondriven condition

To measure more LZRO cycles within an effective coherence time, the driven frequency, ω_s , is set to $2\pi \times 62.5$

Hz (with an LZRO period of 16 ms) under the slow passage limit condition. Under LZ destructive conditions, four periods of oscillation are observed, as shown in Fig. 7. The nondriven modulation Rabi periods are 1 ms and 8.96 ms at $g=320$ Hz and $g=400$ Hz, respectively.

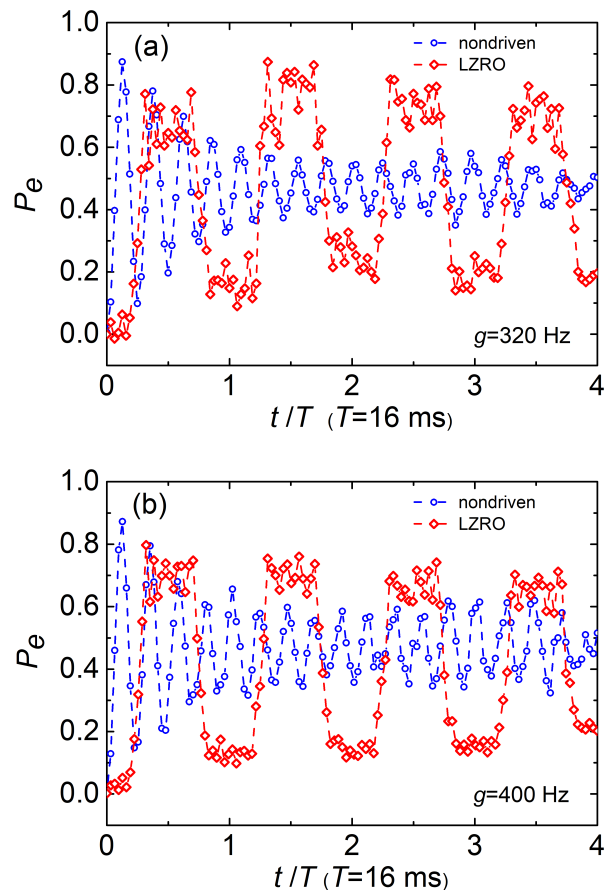


FIG. 7. Rabi oscillations of the LZ and nondriven conditions. Diamond plots in red represent LZRO, while circles in blue represent the nondriven Rabi oscillation spectrum. T denotes oscillation period of LZRO. For $g=320$ Hz, $A=20.6$ in (a), and for $g=400$ Hz, $A=21.4$ in (b), respectively.

[1] Y. Teranishi and H. Nakamura, Control of time-dependent nonadiabatic processes by an external field, *Phys. Rev. Lett.* **81**, 2032 (1998).
 [2] K. Saito and Y. Kayanuma, Nonadiabatic electron manipulation in quantum dot arrays, *Phys. Rev. B* **70**, 201304 (2004).
 [3] L. Gaudreau, G. Granger, A. Kam, G. C. Aers, S. A. Studenikin, P. Zawadzki, M. Pioro-Ladriere, Z. R. Wasilewski, and A. S. Sachrajda, Coherent control of three-spin states in a triple quantum dot, *Nat. Phys.* **8**, 54 (2012).

[4] G. Cao, H.-O. Li, T. Tu, L. Wang, C. Zhou, M. Xiao, G.-C. Guo, H.-W. Jiang, and G.-P. Guo, Ultrafast universal quantum control of a quantum-dot charge qubit using landau-zener-stuckelberg interference, *Nat. Commun.* **4**, 1401 (2013).
 [5] F. Gaitan, Temporal interferometry: A mechanism for controlling qubit transitions during twisted rapid passage with possible application to quantum computing, *Phys. Rev. A* **68**, 052314 (2003).
 [6] L. D. Landau, A theory of energy transfer. 2., *Phys. Z. Sowjetunion* **2**, 46 (1932).

- [7] C. Zener and R. H. Fowler, Non-adiabatic crossing of energy levels, *Proc. R. Soc. Lond. A* **137**, 696 (1932).
- [8] E. C. G. Stückelberg, Theory of inelastic collisions between atoms, *Helv. Phys. Acta* **5**, 369–422 (1932).
- [9] E. Majorana, Atomi orientati in campo magnetico variabile, *Nuovo. Cim.* **9**, 43 (1932).
- [10] J. Rotvig, A. Jauho, and H. Smith, Bloch oscillations, zener tunneling, and wannier-stark ladders in the time-domain, *Phys. Rev. Lett.* **74**, 1831 (1995).
- [11] W. D. Oliver, Y. Yu, J. C. Lee, K. K. Berggren, L. S. Levitov, and T. P. Orlando, Mach-zehnder interferometry in a strongly driven superconducting qubit, *Science* **310**, 1653 (2005).
- [12] M. Sillanpää, T. Lehtinen, A. Paila, Y. Makhlin, and P. Hakonen, Continuous-time monitoring of landau-zener interference in a cooper-pair box, *Phys. Rev. Lett.* **96**, 187002 (2006).
- [13] L. Childress and J. McIntyre, Multifrequency spin resonance in diamond, *Phys. Rev. A* **82**, 033839 (2010).
- [14] Q. Zhang, P. Haenggi, and J. Gong, Two-mode bose-einstein condensate in a high-frequency driving field that directly couples the two modes, *Phys. Rev. A* **77**, 053607 (2008).
- [15] C. S. E. van Ditzhuijzen, A. Tauschinsky, and H. B. v. L. van den Heuvel, Observation of stückelberg oscillations in dipole-dipole interactions, *Phys. Rev. A* **80**, 063407 (2009).
- [16] G. Sun, X. Wen, B. Mao, Y. Yu, J. Chen, W. Xu, L. Kang, P. Wu, and S. Han, Landau-zener-stückelberg interference of microwave-dressed states of a superconducting phase qubit, *Phys. Rev. B* **83**, 180507 (2011).
- [17] J. Zhang, J. Zhang, X. Zhang, and K. Kim, Realization of geometric landau-zener-stückelberg interferometry, *Phys. Rev. A* **89**, 013608 (2014).
- [18] F. Forster, G. Petersen, S. Manus, P. Haenggi, D. Schuh, W. Wegscheider, S. Kohler, and S. Ludwig, Characterization of qubit dephasing by landau-zener-stückelberg-majorana interferometry, *Phys. Rev. Lett.* **112**, 116803 (2014).
- [19] H. Liu, M. Dai, and L. F. Wei, Simulating the landau-zener transitions and landau-zener-stückelberg interferometers with compacted optical waveguides: An invariant method, *Phys. Rev. A* **99**, 013820 (2019).
- [20] J. Lidal and J. Danon, Generation of schrodinger-cat states through photon-assisted landau-zener-stückelberg interferometry, *Phys. Rev. A* **102**, 043717 (2020).
- [21] A. Zenesini, D. Ciampini, O. Morsch, and E. Arimondo, Observation of stückelberg oscillations in accelerated optical lattices, *Phys. Rev. A* **82**, 065601 (2010).
- [22] X. Wang, H. D. Liu, and L. B. Fu, Nonlinear non-hermitian landau-zener-stückelberg-majorana interferometry, *New J. Phys.* **25**, 043032 (2023).
- [23] O. V. Ivakhnenko, S. N. Shevchenko, and F. Nori, Nonadiabatic landau-zener-stückelberg-majorana transitions, dynamics, and interference, *Phys. Rep.-Rev. Sec. Phys. Lett.* **995**, 1 (2023).
- [24] X. Qiao, X.-B. Zhang, Y. Jian, Y.-E. Ma, R. Gao, A.-X. Zhang, and J.-K. Xue, Nonlinear landau-zener-stückelberg-majorana tunneling and interferometry of extended bose-hubbard flux ladders, *Phys. Rev. E* **108**, 034214 (2023).
- [25] S. N. Shevchenko, S. Ashhab, and F. Nori, Landau-zener-stückelberg interferometry, *Phys. Rep.-Rev. Sec. Phys. Lett.* **492**, 1 (2010).
- [26] S. Ashhab, J. R. Johansson, A. M. Zagoskin, and F. Nori, Two-level systems driven by large-amplitude fields, *Phys. Rev. A* **75**, 063414 (2007).
- [27] I. I. Rabi, Space quantization in a gyrating magnetic field, *Phys. Rev.* **51**, 652 (1937).
- [28] D. V. Khomitsky, M. V. Bastrakova, V. O. Munyaev, N. A. Zaprudnov, and S. A. Studenikin, Controllable single-spin evolution at subharmonics of electric dipole spin resonance enhanced by four-level landau-zener-stückelberg-majorana interference, *Phys. Rev. B* **108**, 205404 (2023).
- [29] J. Zhou, P. Huang, Q. Zhang, Z. Wang, T. Tan, X. Xu, F. Shi, X. Rong, S. Ashhab, and J. Du, Observation of time-domain rabi oscillations in the landau-zener regime with a single electronic spin, *Phys. Rev. Lett.* **112**, 010503 (2014).
- [30] A. D. Ludlow, M. M. Boyd, J. Ye, E. Peik, and P. O. Schmidt, Optical atomic clocks, *Rev. Mod. Phys.* **87**, 637 (2015).
- [31] H. Katori, T. Ido, and M. Kuwata-Gonokami, Optimal design of dipole potentials for efficient loading of sr atoms, *J. Phys. Soc. Jpn.* **68**, 2479 (1999).
- [32] W.-X. Liu, T. Wang, X.-F. Zhang, and W.-D. Li, Time-domain landau-zener-stückelberg-majorana interference in an optical lattice clock, *Phys. Rev. A* **104**, 053318 (2021).
- [33] M.-J. Yin, T. Wang, X.-T. Lu, T. Li, Y.-B. Wang, X.-F. Zhang, W.-D. Li, A. Smerzi, and H. Chang, Rabi spectroscopy and sensitivity of a floquet engineered optical lattice clock, *Chin. Phys. Lett.* **38**, 073201 (2021).
- [34] X.-T. Lu, T. Wang, T. Li, C.-H. Zhou, M.-J. Yin, Y.-B. Wang, X.-F. Zhang, and H. Chang, Doubly modulated optical lattice clock: Interference and topology, *Phys. Rev. Lett.* **127**, 033601 (2021).
- [35] Q. Xu, X. Lu, J. Xia, Y. Wang, and H. Chang, Measuring the probe stark shift by frequency modulation spectroscopy in an ^{87}Sr optical lattice clock, *Appl. Phys. Lett.* **119**, 101105 (2021).